Nanoscale

Oxygen incorporated WS2 Nanoclusters with Superior Electrocatalytic Properties for Hydrogen Evolution Reaction

Journal:	*Nanoscale*
Manuscript ID	NR-ART-01-2018-000253.R1
Article Type:	Paper
Date Submitted by the Author:	23-Mar-2018
Complete List of Authors:	Sarma, Prasad; Indian Institute of Science Education & Research Thiruvananthapuram, Physics Tiwary, C.; Rice University, Department of Materials Science and NanoEngineering Radhakrishnan, Sruthi; Rice University, Department of Materials Science and NanoEngineering Ajayan, Pulickel M.; Rice University, Department of Mechanical Engineering & Materials Science Shaijumon, Manikoth; Indian Institute of Science Education & Research Thiruvananthapuram, Physics

SCHOLARONE™
Manuscripts

Please do not adjust margins

Nanoscale

ARTICLE

Oxygen incorporated WS_2 Nanoclusters with Superior Electrocatalytic Properties for Hydrogen Evolution Reaction

Received 00th January 20xx,
Accepted 00th January 20xx

DOI: 10.1039/x0xx00000x

www.rsc.org/

Prasad V. Sarma,[a] Chandra Sekhar Tiwary,[b] Sruthi Radhakrishnan,[b] Pulickel M. Ajayan[b] and Manikoth M. Shaijumon[a,*]

Transition metal dichalcogenides (TMDs) exhibit unique properties and show potential for promising applications in energy conversion. Mono/few-layered TMDs have been widely explored as active electrocatalysts towards hydrogen evolution reaction (HER). Controlled synthesis of TMD nanostructures with unique structural and electronic properties, leading to highly active sites or higher conductivity, is essential to achieve enhanced HER activity. Here, we demonstrate a new approach to controllably synthesize highly catalytically active oxygen-incorporated 1T and 2H WS_2 nanoclusters from oxygen deficient WO_3 nanorods, following chemical exfoliation and ultrasonication processes, respectively. The as-synthesized 1T nanoclusters, with unique properties of tailored edge sites, enhanced conductivity resulting from the metallic 1T phase and oxygen incorporation, have been identified as highly active and promising electrocatalysts for HER, with very low Tafel slope of 47 mV decade^{-1} and low onset overpotential of 88 mV, along with exceptionally high exchange current density and very good stability. The study could be extended to other TMD materials for potential applications in energy conversion and storage.

Introduction

With the increase in global population and the rise in energy consumption, search for clean and efficient alternative energy resources has become important. Hydrogen turns out to be a natural choice, with its eco-friendly nature, and hence achieving efficient routes for its generation is becoming increasingly important. Water splitting is an attractive approach, and there is huge interest in developing highly active and efficient electrocatalysts for the hydrogen evolution reaction (HER). A variety of non-precious materials including nickel-molybdenum alloys,[1] transition metal chalcogenides,[2-4] metal carbides,[5] metal-organic frame works[6] and metal-free catalysts[7-10] have been explored as HER catalysts. Two-dimensional layered transition metal dichalcogenides (TMDs) show promising electrocatalytic properties and have been extensively studied for HER, both theoretically and experimentally.[11-14] Monolayer TMD is found in two polymorphs: trigonal prismatic (2H) and octahedral (1T). Since electronic structure strongly depends on the coordination environment of transition metal and distribution of electrons in the *d* subshell, both 1T and 2H phases show contrasting electronic properties.[15, 16] Importantly, the Fermi level of the transition metals lies within the *d* band, which fulfills one of the criteria for a good electrocatalyst.[17] Several studies have shown that the edge sites of TMDs are most active in electrocatalysis, while the basal planes are catalytically inert.[18-22] Improving basal plane activity and addressing the conductivity issues of TMD-based electrocatalysts has been the focus of several recent studies.[19, 23, 24] For example, making defect-rich TMD nanocrystals is a promising strategy to enhance the density of catalytically active sites.[12, 25] Catalytic efficiency of TMDs has been shown to improve with enhanced conductivity resulting from chemical doping, core-shell nanostructures, graphene composites, *etc*.[26-28] Chemically exfoliated MoS_2 and WS_2 (1T phase) show improved HER performance, owing to enhanced electronic conductivity.[29-31]

Though MoS_2 has been the most extensively explored TMD for HER studies, a comparison of catalytic activity of MX_2 (M=Mo, W; X=S, Se) based on theoretical studies reveals that $MoSe_2$ and WS_2 exhibit the best catalytic activity, wherein both transition metal and chalcogenide edges have the most thermoneutral ΔG_H.[20] WS_2 is relatively less explored for HER, and the metallic polymorph of WS_2 is a promising candidate for hydrogen production. Along with chemical exfoliation, strategies like introducing defects or anions in the lattice will enhance the electronic conductivity that in turn improves proton adsorption.[32, 33] Partial or sub-oxides of metals are known to show metallic conductivity.[34] Hence, incorporation of oxygen in the lattice is an effective way to modify the local structure to improve catalytic HER activity.[32, 35]

Here we present a new approach for the controlled synthesis of highly catalytically active WS_2 nanoclusters for hydrogen evolution reaction. Oxygen incorporated 1T and 2H WS_2 nanoclusters are prepared from oxygen deficient WO_{3-x} nanorods, following chemical exfoliation and ultrasonication processes, respectively. We studied

[a] School of Physics, Indian Institute of Science Education and Research Thiruvananthapuram, Maruthamala PO, Thiruvananthapuram, Kerala, 695551, India. E-mail: shaiju@iisertvm.ac.in
[b] Department of Materials Science and NanoEngineering, Rice University, 6100 Main St, Houston, TX 77005, United States
†Electronic Supplementary Information (ESI) available; See DOI: 10.1039/x0xx00000x

Please do not adjust margins

the HER activity of oxygen-incorporated 1T WS_2 (O-WS_2-1T) and 2H WS_2 (O-WS_2-2H) nanoclusters. The presence of tailored edge sites, and enhanced conductivity resulting from the metallic 1T phase and oxygen incorporation, synergistically contribute to the higher HER activity of O-WS_2-1T compared to O-WS_2-2H, making it a promising electrocatalyst. For comparison, HER studies on 1T and 2H WS_2 nanoclusters synthesized from ball milled WS_2 powder (BM-WS_2) and 1T and 2H nanosheets obtained from WS_2 pristine powder, are presented.

Experimental

Materials

WS_2 pristine powder, n-Butyllithium (1.6 M in Hexane), ammonium paratungstate, citric acid and hexadecylamine were purchased from Sigma Aldrich. H_2S gas is produced by standard Kipps apparatus by using Ferrous Sulfate pellets and 0.5 M HCl.

Synthesis of exfoliated 1T and 2H nanostructures

Synthesis of WO_{3-x} rods: An aqueous solution containing a mixture of 1.32 g of $(NH_4)_{10}W_{12}O_{41}\cdot 7H_2O$ and 2.10 g of citric acid was heated to 120 °C under constant stirring for 4–5 h until a gel was formed, which was allowed to stand overnight. 2.45 g of hexadecyl amine dissolved in ethanol was added as an additive to the gel and stirred for 10 h. The resulting mixture was transferred to a 40 ml Teflon autoclave with a stainless steel protective outer body and heated at 200 °C for 4 days. The product obtained was washed with ethanol, cyclohexane, water and finally with ethanol and dried at room temperature. The synthesized compound is blue in color.

Synthesis of oxygen incorporated WS_2 flakes: As-synthesized WO_{3-x} rods were ground with thiourea and kept inside the tubular furnace and heated to 1000 °C. H_2S gas is allowed to pass through the furnace above 500 °C, and for efficient conversion, temperature was dwelled at 1000 °C for 15 min.

Chemical exfoliation: In chemical exfoliation route, as-synthesized oxygen incorporated WS_2 flakes were kept for Lithium intercalation using 1.6 M n-Butyllithium in Hexane. For efficient intercalation, reaction temperature was set at 100 °C and the procedures were extended for 2 days. After cooling, the material is washed several times with anhydrous n-hexane to remove lithium residue. This intercalated compound is exfoliated in water by mixing and sonicating for an hour using Branson 2510 235W sonicator. This dispersion is centrifuged at 14,000 rpm for 30 min to remove un-exfoliated materials, and the obtained sample is referred as **O-WS_2-1T**.

Sonication followed by refluxing: As-synthesized oxygen incorporated WS_2 flakes were dispersed in Dimethylformamide (DMF) by sonicating for 12 h (6 h of bath sonication using Branson 2510 235W sonicator and 6 h of probe sonication by using Branson Sonifier 250 200W; power used was 90 W), which was later kept for refluxing at 150 °C using an oil bath and condenser set up for 24 h in an inert atmosphere. The boiling pressure during refluxing will break the sheets into smaller particles. After refluxing, the dispersion was centrifuged at 14,000 rpm for 20 min and the obtained sample is named as **O-WS_2-2H**.

Synthesis of WS_2-1T and WS_2-2H from bulk WS_2: WS_2 pristine powder was ball-milled for 6 h at 600 rpm in Argon atmosphere. The obtained powder was chemically exfoliated to obtain 1T NPs (**BM-WS_2-1T**), using n-Butyllithium. 2H NPs (**BM-WS_2-2H**) were obtained by sonicating and refluxing the ball-milled powder. In similar route, WS_2 pristine powder was sonicated and refluxed in DMF to obtain WS_2 2H sheets, and chemically exfoliated to prepare WS_2 1T sheets. In all the cases mentioned above, synthesized dispersion was centrifuged at 15000 rpm for 30 min and the supernatant was collected for further studies.

To obtain nanoclusters from WO_3, bulk WO_3 powder was ball-milled for 6 h in Argon atmosphere and the milled powder was grinded with thiourea and heated to 1000 °C in Argon environment. H_2S gas is allowed to pass through the furnace above 500 °C, and temperature was dwelled at 1000 °C for 15 min. The synthesized compound is named as **WO_3-WS_2**. Later WO_3-WS_2 is chemically exfoliated to obtain 1T nanoclusters and liquid-phase exfoliated to obtain WO_3-WS_2-2H nanoclusters.

Materials Characterization

The samples were characterized by using Atomic Force Microscope (Bruker Edge), Raman spectrometer (XploraPlus confocal Micro Raman) using 632 nm laser, scanning electron microscope (Nova NanoSEM 450), transmission electron microscope (JEM 2100F Field emission microscope, 200 kV) and X-ray photoelectron spectrometer (Scienta Omicron). The diffraction patterns were collected by using an Emperean PANalytical XRD system with reference X-ray illumination as Cu K_α radiation at 0.154 nm.

Electrocatalytic measurements

Au electrode was kept immersed in the prepared dispersion for 12 h to obtain a self-assembly on top of the electrode. Later, the electrode was dried and was used as such for electrocatalytic studies. HER studies have been carried out in 0.5 M H_2SO_4 by using three electrode set up with 3M KCl saturated Ag/AgCl as reference electrode, Pt as the counter electrode. Linear sweep voltammetry has been recorded at a scan rate of 2 mV s^{-1} using Biologic SAS VMP3 workstation. Potentiostatic electrochemical impedance spectroscopy (EIS) measurements for various samples were performed at an overpotential of -200 mV *vs* RHE in 3 electrode setup in 0.5 M H_2SO_4.

IR Correction: To compare the performance of various catalysts, all the polarization curves were corrected for Ohmic losses throughout the system, which include the substrate, catalyst material, and solution resistances. All these resistances constitute the series resistance (R_s) of the measurement which can be obtained from an EIS Nyquist plot. Then the *IR* corrected data is given by $E_{Corrected} = E_{Actual} - IR_s$.

Results and discussion

Oxygen-incorporated 1T WS_2 (O-WS_2-1T) and 2H WS_2 (O-WS_2-2H) nanoclusters were synthesized from oxygen deficient WO_{3-x} nanorods under controlled conditions. WO_{3-x} nanorods were prepared by a hydrothermal process using ammonium paratungstate hydrate, citric acid and hexadecylamine. The obtained nanorods are ~400 nm long with 40-80 nm diameter (Fig. S1A†). Light blue colour observed for the synthesized tungsten oxide nanorods dispersed in ethanol (inset of Fig. S1A†) is indicative of its reduced oxidation state (WO_{3-x}).[34, 36]

This journal is © The Royal Society of Chemistry 20xx

Please do not adjust margins

X-ray diffraction analysis further confirms the presence of WO_{3-x} along with monoclinic phase of WO_3 (Fig. S1B†).[37-39] The Raman spectra recorded for WO_{3-x} nanorods show that the peaks are slightly red-shifted compared to that of pristine WO_3 powder (Fig. S1C†). The peaks observed at 715 cm^{-1} and 806 cm^{-1} for pristine WO_3 correspond to O-W^{6+}-O stretching vibrational modes.[40, 41] XPS analysis of WO_{3-x} sample was also conducted, and the peaks located at 34.6 eV and 36.7 eV correspond to the W-O bond of WO_{3-x}, further confirming the partial reduction and presence of oxygen vacancies in WO_{3-x} (Fig. S1D†).[42, 43] XPS results confirm that the compound exists in WO_{3-x} (0<x<1) phase. The recorded O 1s peaks also indicate the changes in coordination configuration of tungsten with oxygen.[34] Detailed characterization details are mentioned in Supporting Information.

Oxygen incorporated WS_2 nanostructures is obtained from WO_{3-x} nanorods by grinding it with thiourea followed by heating at 1000 °C in presence of H_2S gas (Fig. S2†). With an aim to achieve further improvement in electrocatalytic properties, we synthesized oxygen incorporated 1T and 2H WS_2 nanoclusters with enhanced conductivity and more active sites. Multi-layered WS_2 nanostructures obtained from WO_{3-x} rods (O-WS_2) were chemically exfoliated using n-Butyllithium to yield few-layered oxygen-incorporated 1T nanoclusters (O-WS_2-1T). Upon sonication and refluxing in DMF, O-WS_2 nanoclusters were converted to few-layered oxygen-incorporated 2H WS_2 nanoclusters (O-WS_2-2H).

Transmission electron microscopy (TEM) was used to characterize the morphology of both O-WS_2-1T and O-WS_2-2H nanoclusters. As indicated by the TEM and high-resolution TEM (HRTEM) images (Fig. 1), both the samples show nanoclusters of 8-10 nm in size. Fourier Transform (FFT) patterns demonstrate highly ordered diffraction spots corresponding to the 1T phase (inset of Fig. 1A), while the inset of Fig. 1C shows the Selected Area Electron Diffraction (SAED) pattern of the 2H WS_2 nanoclusters with reflections from various planes clearly indexed. HRTEM images of O-WS_2-1T and O-WS_2-2H are shown in Fig. 1B and 1D, respectively. The HRTEM images of O-WS_2-2H and O-WS_2-1T reveal the respective atomic lattices for both the materials (Fig. 2A, D). O-WS_2-2H nanoclusters follow *a* x *a* atomic arrangement which is very stable and common for trigonal prismatic coordination, while O-WS_2-1T with an atomic arrangement of √3*a* x *a*, show zigzag chain clusterization of W atoms, wherein the atoms are shifted from their equilibrium position because of the Jahn-Teller instability.[2] Line intensity profile for O-WS_2-2H and O-WS_2-1T are given in Fig. 2B and E, respectively, and the difference in atomic arrangement for 1T and 2H polymorphs is evident from the respective line intensity profiles. Similar observation has been reported for 1T and 2H MoS_2 systems previously.[44] The FFT pattern for O-WS_2-2H and O-WS_2-1T are shown in Fig. 2C and F, respectively. EELS elemental mapping was performed which further confirmed the elemental composition and their uniform distribution throughout the surface of nanoclusters (Fig. S3†). The corresponding AFM images and height profiles show flake thickness of ~ 2-2.7 nm, which agrees well with ~3 layer WS_2 (Fig. S4†). For comparison, we synthesized 1T and 2H WS_2 nanoclusters from ball-milled WS_2 flakes (BM-WS_2) by chemical exfoliation (BM-WS_2-1T) and refluxing (BM-WS_2- 2H), respectively (Fig. S5, S7, and S8†). Further, same procedures have been followed to prepare WS_2 1T nanosheets (WS_2-P-1T) and WS_2 2H nanosheets (WS_2-P-2H) from pristine WS_2 flakes (Fig. S6, S7, and S8†). Details of synthesis and characterization are given in experimental section†. Raman spectroscopy measurements were performed on O-WS_2-1T and O-WS_2-2H nanoclusters to confirm the phase identification (Fig. 3A). Raman spectra of as-synthesized WO_{3-x} nanorods, and WS_2 nanostructures obtained from WO_{3-x} rods and BM-WS_2 were also recorded for comparison (Fig. 3A). In addition to the characteristic Raman shifts at 347 cm^{-1} and 414 cm^{-1}, the weak peaks in the

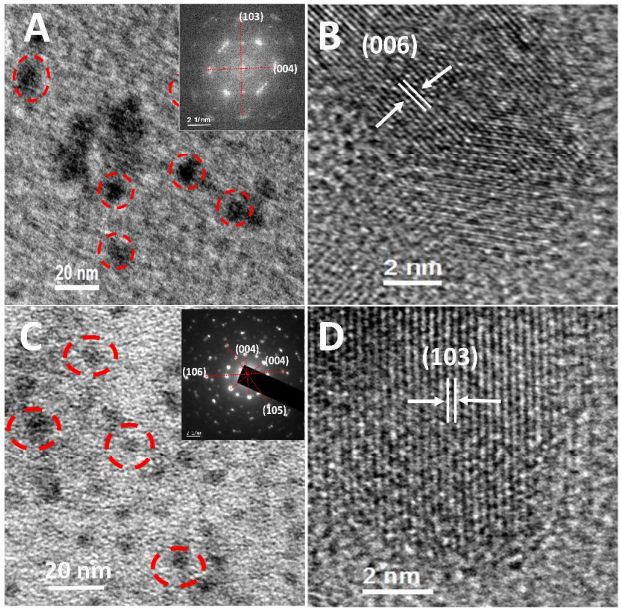

Fig. 1: (A) TEM and (B) high-resolution TEM images of O-WS_2-1T. (C) TEM and (D) HRTEM images of O-WS_2-2H. Inset of (A) shows FFT pattern of O-WS_2-1T, while SAED pattern of O-WS_2-2H is shown as an inset in figure (C). Observed particle dimensions are around 8-10 nm, for both the samples.

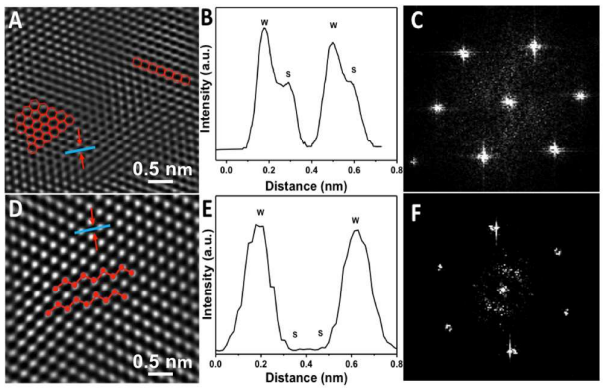

Fig. 2: (A) High-resolution TEM image of O-WS_2-2H. (B) Intensity line profile along the blue line drawn on Figure (A). (C) FFT pattern from O-WS_2-2H. Six-fold coordination symmetry is observed in FFT pattern. (D) HRTEM image of O-WS_2-1T. (E) Intensity line profile along the blue line drawn on Figure (D). (F) FFT pattern from O-WS_2-1T.

Please do not adjust margins

spectrum of O-WS_2 observed at 801 cm^{-1} and 690 cm^{-1} could be due

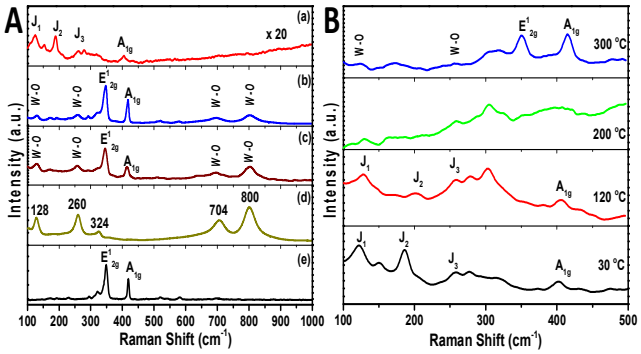

Fig. 3: (A) Raman spectra collected from (a) O-WS_2-1T (b) O-WS_2-2H (c) O-WS_2 (d) WO_{3-x} rods (e) ball milled WS_2 powder (BM-WS_2). (B) Raman spectra recorded for O-WS_2-1T samples annealed in Argon at different temperatures. The Raman peaks for O-WS_2-1T overlap with a W-O peak at 128 cm^{-1}. Raman 1T spectral band intensities are observed to be low compared with the high spectral response from 2H phase WS_2.

to O-W-O vibrations arising from the incorporated oxygen, which is slightly shifted compared to those observed for WO_{3-x} nanorods. The spectrum of O-WS_2-2H shows the characteristic 2H-WS_2 peaks corresponding to E^1_{2g} and A_{1g} at 348 cm^{-1} and 416 cm^{-1}, respectively.[45] In addition to A_{1g} peak, spectrum of O-WS_2-1T exhibits weak peaks in the lower frequency region, referred as J_1, J_2, and J_3, corresponding to the modes that are active only in 1T-WS_2.[46] To confirm the presence of meta-stable 1T phase, we monitored Raman spectra of O-WS_2-1T as a function of annealing temperature (Fig. 3B). The spectra shows that with increase in annealing temperature, the intensities of Raman active modes from the 1T phase decreased, while the characteristic peaks corresponding to the 2H phase became intense. This behavior is due to the structural transformation from octahedral 1T phase to 2H phase at higher temperatures. No changes were observed in the Raman spectra of O-WS_2-2H under similar conditions (Fig. S7C†).

X-ray photoelectron spectroscopy (XPS) is an effective tool to characterize the 2H and 1T polymorphs of TMDs.[47, 48] XPS spectra were collected from both O-WS_2-1T and O-WS_2-2H nanoclusters and are compared with that of bulk WS_2 and WO_{3-x} nanorods. High-resolution XPS spectrum of W 4f for O-WS_2-2H (Fig. 4A) shows two peaks at 34.0 eV and 36.1 eV, corresponding to W $4f_{7/2}$ and W $4f_{5/2}$ of the 2H polymorph, respectively. The shift in signals towards higher binding energies compared to that of bulk 2H WS_2 (Fig. 4B) could be attributed to the presence of incorporated oxygen in the lattice. However, shifted peaks are observed at lower binding energies compared to W^{6+}.[49, 50] O-WS_2-1T exhibited signals corresponding to 1T phase as indicated by the peaks at 31.9 eV and 34 eV (Fig. 4C).[47] Though O-WS_2-1T showed a larger percentage of 1 T phase, the presence of 2H phase was also revealed from the peaks at ~33.1 eV and 35.0 eV. Presence of additional peaks at higher binding energies, 35.4 eV, and 37.45 eV, correspond to surface oxidation during exfoliation in water. XPS spectrum of W 4f for WO_{3-x} nanorods confirmed the presence of W^{5+} species with peaks observed at 34.6 eV and 36.7 eV (Fig. 4D).[43] The S 2p high-resolution spectra also showed similar results indicating the presence of 1T and 2H polymorphs (Fig. S9A, B†) Further, the oxygen incorporation in WS_2 is confirmed by analyzing the O 1s peaks (Fig. S9C, D†). O 1s peaks observed at 530.1 eV and 530.3 eV in O-WS_2-1T and O-WS_2-2H, respectively, correspond to the binding energies of oxygen in W-O bond, confirming the oxygen incorporation.[51, 52] However, the O 1s peak of WO_{3-x} nanorods is found to shift towards lower binding energy (529.3 eV), indicating the presence of oxygen vacancies.[34, 53] The other O 1s peak observed at 531.7 eV could be attributed to the presence of surface adsorbed OH^- species.[54, 55] The atomic oxygen percentage has been calculated from XPS spectra and survey scans (Fig. S10†). Even in bulk material, we detect around 14% of Oxygen, and this is due to the adsorbed species (Fig. S10A†). Ball-milled WS_2 sample also shows similar oxygen percentage to that of pristine WS_2, and further from high-resolution spectra (Fig. S10C†), it was confirmed that BM-WS_2 sample is not oxidized even after ball milling. The presence of oxygen in O-WS_2-1T samples could be quantified from the wide scan and high-resolution spectra (Fig. S10D† and S9C† respectively), and was calculated to be ~8.5% as incorporated oxygen and remaining oxygen as adsorbed species. In a similar way, the presence of oxygen in O-WS_2-2H is calculated as ~9.9%

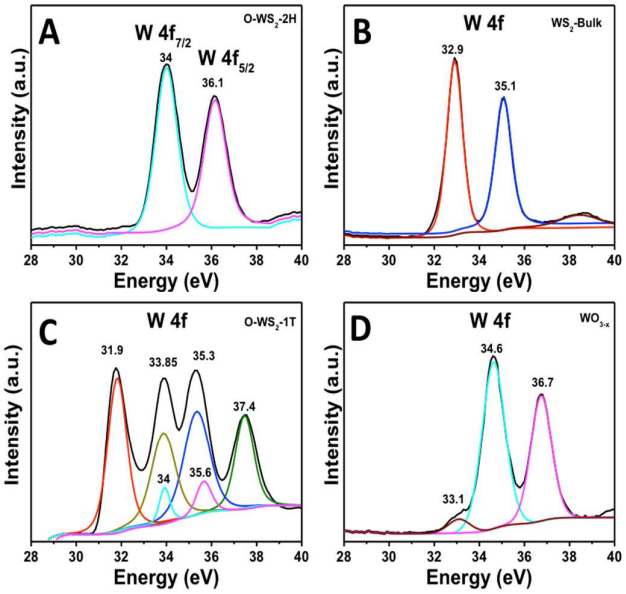

Fig. 4: XPS W 4f spectra collected from (A) O-WS_2-2H (B) WS_2 bulk sample (C) O-WS_2-1T and (D) WO_{3-x} nanorods. In O-WS_2-2H, W 4f peaks, are found to be shifted towards higher energies, compared with bulk WS_2, due to the presence of incorporated oxygen in the lattice.

incorporated oxygen and rest as adsorbed species (Fig. S10G† and S9D†). WS_2-P-1T also shows the presence of oxygen (Fig. S10H†). The de-convoluted O1s peak at 530.9 eV in BM-WS_2-1T (Fig. S10F†) and 530.7 eV in WS_2-P-1T (Fig. S10I†) might be due to the formation of trace amount of WO_3 during exfoliation in water.[53, 56]

This journal is © The Royal Society of Chemistry 20xx

Please do not adjust margins

Table 1: Comparison of electrocatalytic activity towards HER for various WS_2 catalysts studied

Starting Material	Method/ Sample	Tafel slope (mV dec^{-1})	Onset potential to attain 10 mA cm^{-2}	Exchange Current density (mA cm^{-2})
WS2 pristine powder	Chemically lithiated and exfoliated in DI water/ (**WS_2-P-1T**)	78	-208	3.2 x 10^{-3}
	Refluxed in DMF at 150 °C for 24 h /(**WS_2-P-2H**)	90	-332	1.0 x 10^{-4}
WS_2 from WO_{3-x} nanorods (O-WS_2)	Chemically lithiated and exfoliated in DI water / (**O-WS_2-1T**)	47	-88	2.2 x 10^{-2}
	Refluxed in DMF at 150 °C for 24 h / (**O-WS_2-2H**)	79	-176	7.0 x 10^{-3}
WS_2 Pristine powder ball-milled in Argon for 6 h (WS_2-BM)	Chemically lithiated and exfoliated in DI water/(**BM-WS_2-1T**)	57	-110	1.12 x 10^{-2}
	Refluxed in DMF at 150 °C for 24 h / (**BM-WS_2-2H**)	80	-283	1.3 x 10^{-3}

Oxygen content (%), dimensions, and edge to the basal plane ratio (in %) of various catalysts studied are given in Table S1. The presence of tailored edge sites, and enhanced conductivity resulting from the metallic 1T phase and oxygen incorporation, as revealed from the above analyses, could lead to efficient electrocatalytic activity for O-WS_2-1T and O-WS_2-2H.

Electrocatalytic Studies

To investigate the HER activity, electrochemical measurements were performed on O-WS_2-1T and O-WS_2-2H nanoclusters. Nanoclusters self-assembled on Au rods have been used as working electrode, considering the strong binding of TMDs onto Au substrates.[57] We carried out linear sweep voltammetry (LSV) measurements on all the samples in 0.5 M H_2SO_4 in a 3-electrode setup by using Ag/AgCl as a reference electrode and Pt as the counter electrode. All measurements were performed under the same optimized experimental conditions. The iR corrected polarization curves for oxygen-incorporated 1T, and 2H WS_2 nanoclusters are shown in Fig. 5A. All the WS_2 nanostructures studied exhibited lower onset potentials (η) compared to bulk WS_2 and Au substrate. O-WS_2-1T showed the lowest onset potential of 88 mV, revealing the best HER activity.

It is evident that oxygen incorporation in WS_2 nanoclusters has led to excellent HER activity for O-WS_2-1T and O-WS_2-2H nanoclusters compared to pristine nanoclusters and nanosheets. To obtain further insight into the electrocatalytic activity, Tafel slopes were measured from the linear region of the Tafel plots, which are derived from LSV polarization curves (Fig. 5B). Tafel slope is an important indicator of HER activity, smaller values indicating faster HER rates. The corresponding Tafel plots further reveal that the nanoclusters with oxygen incorporation possess smaller Tafel slopes of 47 and 79 mV $decade^{-1}$ for O-WS_2-1T and O-WS_2-2H, respectively. The obtained Tafel slope of 47 mV $decade^{-1}$ for O-WS_2-1T is very close to that of Pt (35 mV $decade^{-1}$) measured under similar experimental conditions. In-order to understand the effect of improved edge to basal plane ratio upon their electrocatalytic activity, we studied the HER activity of few-layered 1T WS_2 nanosheets synthesized *via* chemical lithiation of WS_2 pristine powder, followed by exfoliation in DI water (WS_2-P-1T). Further, few-layered 2H WS_2 nanosheets (WS_2-P-2H) obtained by refluxing

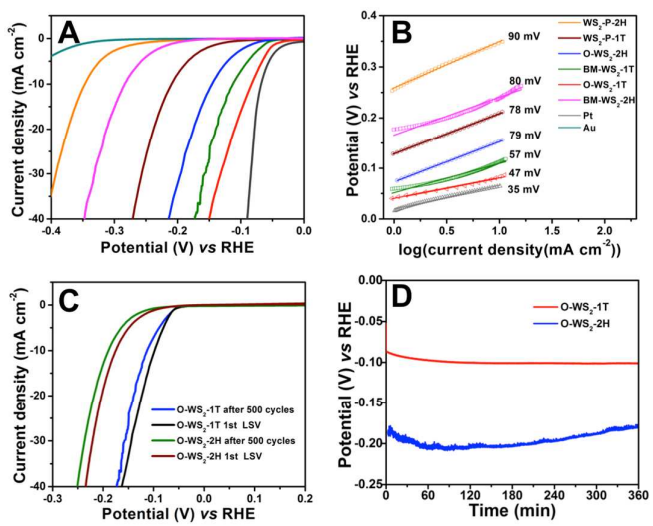

Fig. 5: Electrochemical characterization of oxygen-incorporated WS_2 nanoclusters. (A) Polarization curves obtained for O-WS_2-1T and O-WS_2-2H -modified Au electrodes measured at a scan rate of 2 mV sec^{-1} in 0.5 M aq. H_2SO_4 electrolyte. Polarization curves obtained for BM-WS_2-2H, BM-WS_2 -1T, WS_2-P-2H, WS_2-P-1T –modified Au electrodes along with bare Au and Pt electrodes are shown for comparison. (B) Tafel plots obtained from O-WS_2-1T, O-WS_2-2H, WS_2-BM-2H, WS_2-BM-1T nanoclusters, WS_2-P-2H and WS_2-P-1T sheets. O-WS_2-1T shows better performance followed by WS_2-BM-1T. (C) Polarization curve of O-WS_2-1T and O-WS_2-2H electrocatalysts after 1st and 500 HER cycles. (D) Stability plots from O-WS_2-1T and O-WS_2-2H-modified Au electrodes, wherein constant current of 10 mA cm^{-2} are continuously drawn from the system, and the potential required to drive the reaction is monitored.

WS_2 pristine powder in DMF at 150 °C for 24 h, was also studied for their HER activity. While WS_2-P-1T showed an onset potential of 208 mV, owing to its metallic behaviour, WS_2-P-2H exhibited an

Please do not adjust margins

Table 2: Comparison of electrocatalytic HER performances of WS_2 catalysts reported so far

Catalyst & morphology	Synthesis	Onset potential (mV)	Tafel slope (mV/dec)	J_0 (mA cm^{-2})
WS_2-rGO hybrid nanosheets [25]	Hydrothermal process	150	58	--
WS_2-1T sheets [28]	Chemical exfoliation	100	55	2.0 x 10^{-2}
WS_2-1T sheets [29]	Chemical exfoliation	-142	70	--
WS_2 nanosheets [62]	Mechanical activation by ball milling	-150	72	2.5 x 10^{-3}
WS_2 nanoflakes [63]	CVD thermolysis process	200	78	5.8 x 10^{-3}
WS_2 nanoflakes [61]	High temperature solution- phase synthesis	100	48	--
WS_2/graphene/Ni 3D structure [55]	Hydrothermal process	87	79	--
WS_2 nanoplates anchored to hollow nitrogen-doped carbon nanofibers [56]	Coaxial electrospinning	90	60	--
WS_2/graphene/Ni foam [64]	Thermal de-composition of precursors	119	43	--
WS_2-rGO composite [65]	Hydrothermal process	150	58	--
O-WS_2-1T (**Present work**)	Chemically lithiated and exfoliated in DI water	88	47	2.2 x 10^{-2}

onset potential of 332 mV (Fig. 5A). The obtained Tafel slopes of 78 mV $decade^{-1}$ and 90 mV $decade^{-1}$, respectively, for WS_2-P-1T and WS_2-P-2H, are higher than that of O-WS_2-1T and O-WS_2-2H nanoclusters. This indicates the role of enhanced edge sites leading to improved HER activity in O-WS_2-1T and O-WS_2-2H nanoclusters. To further look into the role of oxygen incorporation in these nanoclusters for their improved HER activity, controlled experiments have been performed on BM-WS_2-1T, and BM-WS_2-2H nanoclusters (without oxygen incorporation), which are obtained from ball-milled WS_2 pristine powder *via* chemical exfoliation and refluxing procedures, respectively. The size of the obtained nanoclusters was comparable to that of O-WS_2-1T and O-WS_2-2H (Fig. S5†). Hence, a comparison study of the electrocatalytic properties of BM-WS_2-1T and BM-WS_2-2H will reveal the effect of oxygen incorporation in such nanoclusters upon their HER activity. BM-WS_2-1T exhibited improved onset potential of 110 mV, whereas BM-WS_2-2H showed an onset potential of 283 mV, which is much better than their nanosheet counterparts, owing to the improved edge sites. Tafel slopes of 57 mV $decade^{-1}$ and 80 mV $decade^{-1}$ were calculated for BM-WS_2-1T and BM-WS_2-2H, respectively, which are found to be better compared to pristine WS_2 and WS_2 nanosheets. Thus the obtained onset potential of 88 mV and Tafel slope of 47 mV $decade^{-1}$ for O-WS_2-1T are the best among all the materials studied here and are record values for WS_2 electrocatalysts, to the best of our knowledge.[58, 59]

Analyzing the HER mechanism in acidic media, one of the following routes are involved in the generation of molecular hydrogen.[60]

$$\text{Volmer: } H_2O + e^- \leftrightarrow H(ads) + OH^-$$

$$\text{Heyrovsky: } H_2O + H(ads) + e^- \leftrightarrow H_2(g) + OH^-$$

$$\text{Tafel: } H(ads) + H(ads) \leftrightarrow H_2(g)$$

While the measured Tafel slope of 35 mV $decade^{-1}$ for Pt indicates a fast Volmer-Tafel reaction, a Tafel slope of 47 mV $decade^{-1}$ for O-WS_2-1T suggest a fast HER *via* Volmer-Heyrovsky process.[61] The obtained Tafel slopes of 80 mV $decade^{-1}$ and 90 mV $decade^{-1}$ for BM-WS_2-2H and WS_2-P-2H, respectively, indicate Volmer reaction as the rate-limiting step.[11, 62] Potentiostatic EIS spectra of various samples were conducted at an overpotential of -200 mV *vs* SHE in 3 electrode setup in 0.5M H_2SO_4 and the PEIS plot is shown in Fig. S11†. Charge transfer resistance of various catalysts were measured (Table S1†) and found that O-WS_2-1T illustrates least charge transfer resistance in the catalytically active regime.

Exchange current density (j_o) is another key parameter that suggests better HER activity of the electrocatalyst. O-WS_2-1T exhibits very high exchange current density of 2.2 x 10^{-2} mA cm^{-2}, which is twice larger than BM-WS_2-1T and one order larger than all other samples studied here (Table 1). The remarkably large value obtained for O-WS_2-1T indicate excellent HER activity of the electrocatalyst and is among the best-reported values for TMD based electrocatalysts (Table 2).[26, 29, 30, 58, 63-68]

This journal is © The Royal Society of Chemistry 20xx

Please do not adjust margins

Stability of the electrocatalyst is very important for practical applications. Both the electrocatalysts showed good cycling stability after 500 cycles (Fig. 5C). The electrochemical stability of O-WS_2-1T and O-WS_2-2H nanoclusters were further studied by using chronopotentiometry technique by continuously monitoring the overpotential while a constant current of 10 mA cm^{-2} is drawn from the system (Fig. 5D). While the measured overpotential remains very stable for O-WS_2-1T, the overpotential is found to be stable in 6 h for O-WS_2-2H, after a slight decrease in the beginning. We conducted several experiments to calculate the electrochemical surface area (ECSA) of the electrocatalysts. Detailed experimental procedures are narrated in supporting information (section 4), where ECSA is calculated using Randles-Sevcik equation (Fig. S12, 13†, Table S2) and electric double layer capacitance methods (Fig. S15†, Table S3). In-order to understand the intrinsic activity of the electrocatalysts, the polarization curves are replotted based on the electrochemical surface area (Fig. S14,16†). To compare the intrinsic activity, we calculated exchange current density from ECSA normalized polarization curve (Table S4) and found that O-WS_2-1T catalyst exhibited highest exchange current density of 2.5 x 10^{-2} mA cm^{-2}, compared to all other catalysts studied.

The excellent HER activity exhibited by O-WS_2-1T nanoclusters can be attributed to a combination of multiple factors such as metallic nature of 1T phase, enhanced edge to basal plane ratio arising from defect-rich nanoclusters, improved conductivity upon oxygen incorporation.[32] The improved conductivity of O-WS_2-1T nanoclusters is well reflected in their exchange current densities, which is two times larger compared to 1T nanoclusters of similar dimensions, without oxygen incorporation (BM-WS_2-1T). We followed a novel approach to obtain oxygen-incorporated WS_2 nanoclusters from oxygen deficient WO_3, taking advantage of the fact that it is difficult to sulfurize oxygen deficient WO_3 completely, even at 1000 °C,[65] thus resulting in the formation of oxygen incorporated WS_2. To confirm the effect of partial oxides involved in the synthesis step, we synthesized WS_2 from ball-milled WO_3 pristine powder (WO_3-WS_2), detailed characterization is given in supporting information **(**Fig. S17†**)**. In comparison to O-WS_2, W-O Raman vibration modes are nearly vanished in WO_3-WS_2, confirming the complete formation of WS_2 phase (Fig. S17F†). Further, few-layered nanoclusters obtained from WO_3-WS_2 by chemical exfoliation (WO_3-WS_2-1T) and liquid phase exfoliation (WO_3-WS_2-2H), with similar dimensions (Fig. S17**,** S18, and S19†), exhibited much lower electrocatalytic activity compared to O-WS_2-1T and O-WS_2-2H. The incorporated oxygen in the lattice enhances the conductivity of the material, and also provide active centers for catalysis. The combined effect of metallic behaviour and presence of incorporated oxygen in the lattice thus leads to the superior HER performance of the electrocatalyst. For comparison, HER studies have been performed on pristine samples. The polarization and Tafel plots obtained from WO_3 pristine, WS_2 pristine powder, WO_{3-x} rods and O-WS_2 nanoflakes drop casted on to glassy carbon substrates are shown in supporting Fig. S 20†.

Conclusions

In summary, we have demonstrated a novel approach to synthesize highly catalytically active oxygen-incorporated 1T and 2H WS_2 nanoclusters from oxygen deficient WO_3 nanorods, following chemical exfoliation and ultrasonication processes, respectively. O-WS_2-1T and O-WS_2-2H nanoclusters have been explored as active electrocatalysts for HER in acidic solution. The as-synthesized O-WS_2-1T nanoclusters, with unique properties of tailored edge sites, enhanced conductivity resulting from the metallic 1T phase and oxygen incorporation, have been identified as highly active and promising electrocatalyst for HER, with very low Tafel slope of 47 mV $decade^{-1}$ and with the activity maintained for more than 6 h. For comparison, HER studies on 1T and 2H WS_2 nanoclusters synthesized from ball-milled WS_2 powder (BM-WS_2) and 1T and 2H nanosheets obtained from WS_2 pristine powder, were performed. This study thus brings out a facile route for the controlled synthesis of WS_2 based active electrocatalysts with unique intrinsic properties, which could be extended to other TMD materials for potential applications in energy conversion and storage.

Conflicts of interest

There are no conflicts to declare

Acknowledgements

PVS acknowledges UGC, Govt. of India for the financial Support. MMS acknowledge financial support from Science and Engineering Research Board (SERB), Department of Science & Technology, Govt. Of India (EMR/2017/000484) and Indian Institute of Science Education and Research (IISER) Thiruvananthapuram, Kerala, INDIA. S.R and P.M.A. thank the support from Air Force Office of Scientific Research (AFOSR) Grant No. FA9550-12-1-0035.

References

1. L. Chen and A. Lasia, *J. Electrochem. Soc.*, 1992, **139**, 3458-3464.
2. M. Chhowalla, H. S. Shin, G. Eda, L.-J. Li, K. P. Loh and H. Zhang, *Nat Chem*, 2013, **5**, 263-275.
3. J. Yang and H. S. Shin, *J. Mater. Chem. A*, 2014, **2**, 5979-5985.
4. D. Gopalakrishnan, D. Damien, B. Li, H. Gullappalli, V. K. Pillai, P. M. Ajayan and M. M. Shaijumon, *Chem. Commun.*, 2015, **51**, 6293-6296.
5. R. Michalsky, Y.-J. Zhang and A. A. Peterson, *ACS Catal.*, 2014, **4**, 1274-1278.
6. D. Grumelli, B. Wurster, S. Stepanow and K. Kern, *Nat Commun*, 2013, **4**.
7. Y. Zheng, Y. Jiao, Y. Zhu, L. H. Li, Y. Han, Y. Chen, A. Du, M. Jaroniec and S. Z. Qiao, *Nat Commun*, 2014, **5**.
8. G. F. Moore and I. D. Sharp, *J. Phys. Chem. Lett.*, 2013, **4**, 568-572.
9. S. Pal, M. Sahoo, V. T. Veettil, K. K. Tadi, A. Ghosh, P. Satyam, R. K. Biroju, P. M. Ajayan, S. K. Nayak and T. N. Narayanan, *ACS Catal.*, 2017, **7**, 2676-2684.
10. S. Kundu, B. Malik, D. K. Pattanayak, R. Pitchai and V. K. Pillai, *ChemistrySelect*, 2017, **2**, 4511-4515.
11. Q. Tang and D.-e. Jiang, *ACS Catalysis*, 2016, **6**, 4953-4961.
12. Z. Wu, B. Fang, Z. Wang, C. Wang, Z. Liu, F. Liu, W. Wang, A. Alfantazi, D. Wang and D. P. Wilkinson, *ACS Catal*, 2013, **3**, 2101-2107.
13. J. Wang, J. Liu, B. Zhang, X. Ji, K. Xu, C. Chen, L. Miao and J. Jiang, *Phys. Chem. Chem. Phys.*, 2017, **19**, 10125-10132.
14. D. Gopalakrishnan, D. Damien and M. M. Shaijumon, *ACS Nano*, 2014, **8**, 5297-5303.

Please do not adjust margins

15. U. Gupta, B. S. Naidu, U. Maitra, A. Singh, S. N. Shirodkar, U. V. Waghmare and C. N. R. Rao, *APL Mater.*, 2014, **2**, 092802.
16. T. Xiang, Q. Fang, H. Xie, C. Wu, C. Wang, Y. Zhou, D. Liu, S. Chen, A. Khalil, S. Tao, Q. Liu and L. Song, *Nanoscale*, 2017, **9**, 6975-6983.
17. P. Quaino, F. Juarez, E. Santos and W. Schmickler, *Beilstein J. Nanotechnol.*, 2014, **5**, 846-854.
18. J. Kibsgaard, Z. Chen, B. N. Reinecke and T. F. Jaramillo, *Nat Mater*, 2012, **11**, 963-969.
19. H. Li, C. Tsai, A. L. Koh, L. Cai, A. W. Contryman, A. H. Fragapane, J. Zhao, H. S. Han, H. C. Manoharan, F. Abild-Pedersen, J. K. Norskov and X. Zheng, *Nat Mater*, 2016, **15**, 48-53.
20. C. Tsai, K. Chan, F. Abild-Pedersen and J. K. Norskov, *Phys. Chem. Chem Phys*, 2014, **16**, 13156-13164.
21. G. Babu, N. Masurkar, H. Al Salem and L. M. R. Arava, *J. Am. Chem. Soc.*, 2017, **139**, 171-178.
22. A. Winchester, S. Ghosh, S. Feng, A. L. Elias, T. Mallouk, M. Terrones and S. Talapatra, *ACS Appl. Mater. Interfaces*, 2014, **6**, 2125-2130.
23. Y. Ouyang, C. Ling, Q. Chen, Z. Wang, L. Shi and J. Wang, *Chem. Mater.*, 2016, **28**, 4390-4396.
24. R. K. Biroju, D. Das, R. Sharma, S. Pal, L. P. L. Mawlong, K. Bhorkar, P. K. Giri, A. K. Singh and T. N. Narayanan, *ACS Energy Lett.*, 2017, **2**, 1355-1361.
25. G. Ye, Y. Gong, J. Lin, B. Li, Y. He, S. T. Pantelides, W. Zhou, R. Vajtai and P. M. Ajayan, *Nano Letters*, 2016, **16**, 1097-1103.
26. J. Zhang, Q. Wang, L. Wang, X. a. Li and W. Huang, *Nanoscale*, 2015, **7**, 10391-10397.
27. X. Ren, Q. Ma, H. Fan, L. Pang, Y. Zhang, Y. Yao, X. Ren and S. Liu, *Chem. Commun.*, 2015, **51**, 15997-16000.
28. Z. Chen, D. Cummins, B. N. Reinecke, E. Clark, M. K. Sunkara and T. F. Jaramillo, *Nano Lett.*, 2011, **11**, 4168-4175.
29. D. Voiry, H. Yamaguchi, J. Li, R. Silva, D. C. B. Alves, T. Fujita, M. Chen, T. Asefa, V. B. Shenoy, G. Eda and M. Chhowalla, *Nat Mater*, 2013, **12**, 850-855.
30. M. A. Lukowski, A. S. Daniel, C. R. English, F. Meng, A. Forticaux, R. J. Hamers and S. Jin, *Energy Environ. Sci.*, 2014, **7**, 2608-2613.
31. Q. He, Y. Wan, H. Jiang, C. Wu, Z. Sun, S. Chen, Y. Zhou, H. Chen, D. Liu, Y. A. Haleem, B. Ge, X. Wu and L. Song, *Nano Research*, 2018, **11**, 1687-1698.
32. J. Xie, J. Zhang, S. Li, F. Grote, X. Zhang, H. Zhang, R. Wang, Y. Lei, B. Pan and Y. Xie, *J. Am. Chem. Soc*, 2013, **135**, 17881-17888.
33. X. She, J. Wu, J. Zhong, H. Xu, Y. Yang, R. Vajtai, J. Lou, Y. Liu, D. Du, H. Li and P. M. Ajayan, *Nano Energy*, 2016, **27**, 138-146.
34. Z. Luo, R. Miao, T. D. Huan, I. M. Mosa, A. S. Poyraz, W. Zhong, J. E. Cloud, D. A. Kriz, S. Thanneeru, J. He, Y. Zhang, R. Ramprasad and S. L. Suib, *Adv. Energy Mater.*, 2016, **6**, 1600528-n/a.
35. A. Liu, L. Zhao, J. Zhang, L. Lin and H. Wu, *ACS Appl. Mater. Interfaces*, 2016, **8**, 25210-25218.
36. K. Manthiram and A. P. Alivisatos, *Journal of the American Chemical Society*, 2012, **134**, 3995-3998.
37. Y. A. Barabanenkov, N. D. Zakharov, I. P. Zibrov, V. P. Filonenko, P. Werner, A. I. Popov and M. D. Valkovskii, *Acta Cryst. Sec B*, 1993, **49**, 169-171.
38. J. Booth, T. Ekström, E. Iguchi and R. J. D. Tilley, *Journal of Solid State Chemistry*, 1982, **41**, 293-307.
39. M. Sundberg, N. D. Zakharov, I. P. Zibrov, Y. A. Barabanenkov, V. P. Filonenko and P. Werner, *Acta Cryst. B*, 1993, **49**, 951-958.
40. F. Liu, X. Chen, Q. Xia, L. Tian and X. Chen, *RSC Adv.*, 2015, **5**, 77423-77428.
41. L. Xu, M.-L. Yin and S. Liu, *Sci. Rep.*, 2014, **4**, 6745.
42. M. Remškar, J. Kovac, M. Viršek, M. Mrak, A. Jesih and A. Seabaugh, *Adv. Funct. Mater.* , 2007, **17**, 1974-1978.
43. M. Seifollahi Bazarjani, M. Hojamberdiev, K. Morita, G. Zhu, G. Cherkashinin, C. Fasel, T. Herrmann, H. Breitzke, A. Gurlo and R. Riedel, *J. Am. Chem. Soc.*, 2013, **135**, 4467-4475.
44. S. S. Chou, N. Sai, P. Lu, E. N. Coker, S. Liu, K. Artyushkova, T. S. Luk, B. Kaehr and C. J. Brinker, *Nat. Commun.*, 2015, **6**, 8311.
45. A. Berkdemir, H. R. Gutiérrez, A. R. Botello-Méndez, N. Perea-López, A. L. Elías, C.-I. Chia, B. Wang, V. H. Crespi, F. López-Urías, J.-C. Charlier, H. Terrones and M. Terrones, *Sci. Rep.*, 2013, **3**, 1755.
46. Q. Liu, X. Li, Z. Xiao, Y. Zhou, H. Chen, A. Khalil, T. Xiang, J. Xu, W. Chu, X. Wu, J. Yang, C. Wang, Y. Xiong, C. Jin, P. M. Ajayan and L. Song, *Adv. Mater.*, 2015, **27**, 4837-4844.
47. T. A. J. Loh and D. H. C. Chua, *The Journal of Physical Chemistry C*, 2015, **119**, 27496-27504.
48. A. Ambrosi, Z. Sofer and M. Pumera, *Chem. Commun*, 2015, **51**, 8450-8453.
49. N. V. Alov, *phys. status solidi (c)*, 2015, **12**, 263-266.
50. S. Rahimnejad, J. H. He, W. Chen, K. Wu and G. Q. Xu, *RSC Adv.*, 2014, **4**, 62423-62429.
51. F. Zhan, Y. Yang, W. Li, J. Li, W. Liu, Y. Li and Q. Chen, *RSC Adv.*, 2016, **6**, 10393-10400.
52. A. Tocchetto and A. Glisenti, *Langmuir*, 2000, **16**, 2642-2650.
53. N. Minh Vuong, D. Kim and H. Kim, *Sci. Rep.*, 2015, **5**, 11040.
54. G. E. Buono-Core, A. H. Klahn, C. Castillo, E. Muñoz, C. Manzur, G. Cabello and B. Chornik, *Journal of Non-Crystalline Solids*, 2014, **387**, 21-27.
55. R. F. Garcia-Sanchez, T. Ahmido, D. Casimir, S. Baliga and P. Misra, *J. Phys. Chem. A*, 2013, **117**, 13825-13831.
56. L.-N. Jin, P. Liu, C. Jin, J.-N. Zhang and S.-W. Bian, *Journal of Colloid and Interface Science*, 2018, **510**, 1-11.
57. D. Damien, A. Anil, D. Chatterjee and M. M. Shaijumon, *J. Mater. Chem. A*, 2017, **5**, 13364-13372.
58. F. Qi, P. Li, Y. Chen, B. Zheng, J. Liu, J. Zhou, J. He, X. Hao and W. Zhang, *International Journal of Hydrogen Energy*, 2017, **42**, 7811-7819.
59. S. Yu, J. Kim, K. R. Yoon, J.-W. Jung, J. Oh and I.-D. Kim, *ACS Appl. Mater. Interfaces*, 2015, **7**, 28116-28121.
60. M. R. G. de Chialvo and A. C. Chialvo, *Journal of Electroanalytical Chemistry*, 1994, **372**, 209-223.
61. L. Liao, J. Zhu, X. Bian, L. Zhu, M. D. Scanlon, H. H. Girault and B. Liu, *Adv. Funct. Mater.*, 2013, **23**, 5326-5333.
62. B. E. Conway and B. V. Tilak, *Electrochimica Acta*, 2002, **47**, 3571-3594.
63. L. Yang, X. Zhu, S. Xiong, X. Wu, Y. Shan and P. K. Chu, *ACS Appl. Mater. Interfaces,*, 2016, **8**, 13966-13972.
64. L. Cheng, W. Huang, Q. Gong, C. Liu, Z. Liu, Y. Li and H. Dai, *Angew. Chem. Int. Ed*, 2014, **53**, 7860-7863.

This journal is © The Royal Society of Chemistry 20xx

Please do not adjust margins

65. Z. Wu, B. Fang, A. Bonakdarpour, A. Sun, D. P. Wilkinson and D. Wang, *Applied Catalysis B: Environmental*, 2012, **125**, 59-66.
66. T.-Y. Chen, Y.-H. Chang, C.-L. Hsu, K.-H. Wei, C.-Y. Chiang and L.-J. Li, *Int. J. Hydrogen Energy* 2013, **38**, 12302-12309.
67. H. Zhou, F. Yu, J. Sun, R. He, Y. Wang, C. F. Guo, F. Wang, Y. Lan, Z. Ren and S. Chen, *J. Mater. Chem. A,*, 2016, **4**, 9472-9476.
68. J. Yang, D. Voiry, S. J. Ahn, D. Kang, A. Y. Kim, M. Chhowalla and H. S. Shin, *Angew. Chem. Int. Ed.* , 2013, **52**, 13751-13754.

This journal is © The Royal Society of Chemistry 20xx

Please do not adjust margins

Table of Contents Entry

Oxygen incorporated WS_2 Nanoclusters with Superior Electrocatalytic Properties for Hydrogen Evolution Reaction

*Prasad V. Sarma,[1] Chandra Sekhar Tiwary,[2] Sruthi Radhakrishnan,[2] Pulickel M. Ajayan[2] and Manikoth M. Shaijumon[1,]**
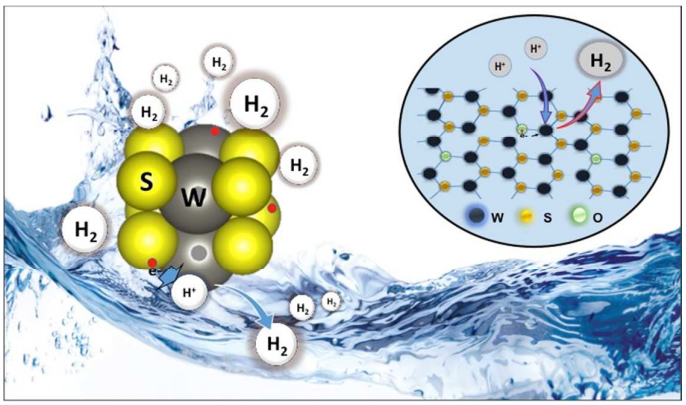
A new approach for the controlled synthesis of oxygen incorporated 1T and 2H WS_2 nanoclusters from oxygen deficient WO_{3-x} nanorods is demonstrated for efficient hydrogen evolution reaction.